

Supporting clinical decision making during deep brain stimulation surgery by means of a stochastic dynamical model

This content has been downloaded from IOPscience. Please scroll down to see the full text.

2014 J. Neural Eng. 11 056019

(<http://iopscience.iop.org/1741-2552/11/5/056019>)

View [the table of contents for this issue](#), or go to the [journal homepage](#) for more

Download details:

This content was downloaded by: sofiak

IP Address: 147.102.131.199

This content was downloaded on 23/09/2014 at 05:28

Please note that [terms and conditions apply](#).

Supporting clinical decision making during deep brain stimulation surgery by means of a stochastic dynamical model

Sofia D Karamintziou^{1,5}, George L Tsirogiannis¹, Pantelis G Stathis²,
George A Tagaris³, Efstathios J Boviatsis^{4,6}, Damianos E Sakas⁴ and
Konstantina S Nikita^{1,5}

¹Biomedical Simulations and Imaging Laboratory, School of Electrical and Computer Engineering, National Technical University of Athens, 9 Iroon Polytechniou Str., 15780 Athens, Greece

²Department of Neurology, 'Agi Anargiri' General Oncological Hospital of Kifissia, 145 Kaliftaki Str., 14564 Athens, Greece

³Department of Neurology, 'G. Gennimatas' General Hospital of Athens, 154 Mesogeion Avenue, 11527 Athens, Greece

⁴Department of Neurosurgery, University of Athens Medical School, 'Evangelismos' General Hospital, 45-47 Ipsilantou Str., 10675 Athens, Greece

E-mail: skaram@biosim.ntua.gr and knikita@ece.ntua.gr

Received 15 March 2014, revised 23 June 2014

Accepted for publication 25 July 2014

Published 22 September 2014

Abstract

Objective. During deep brain stimulation (DBS) surgery for the treatment of advanced Parkinson's disease (PD), microelectrode recording (MER) in conjunction with functional stimulation techniques are commonly applied for accurate electrode implantation. However, the development of automatic methods for clinical decision making has to date been characterized by the absence of a robust single-biomarker approach. Moreover, it has only been restricted to the framework of MER without encompassing intraoperative macrostimulation. Here, we propose an integrated series of novel single-biomarker approaches applicable to the entire electrophysiological procedure by means of a stochastic dynamical model. *Approach.* The methods are applied to MER data pertinent to ten DBS procedures. Considering the presence of measurement noise, we initially employ a multivariate phase synchronization index for automatic delineation of the functional boundaries of the subthalamic nucleus (STN) and determination of the acceptable MER trajectories. By introducing the index into a nonlinear stochastic model, appropriately fitted to pre-selected MERs, we simulate the neuronal response to periodic stimuli (130 Hz), and examine the Lyapunov exponent as an indirect indicator of the clinical effectiveness yielded by stimulation at the corresponding sites. *Main results.* Compared with the gold-standard dataset of annotations made intraoperatively by clinical experts, the STN detection methodology demonstrates a false negative rate of 4.8% and a false positive rate of 0%, across all trajectories. Site eligibility for implantation of the DBS electrode, as implicitly determined through the Lyapunov exponent of the proposed stochastic model, displays a sensitivity of 71.43%. *Significance.* The suggested comprehensive method exhibits remarkable performance in automatically determining both the acceptable MER trajectories and the optimal stimulation sites, thereby having the potential to accelerate precise target finalization during DBS surgery for PD.

⁵ Authors to whom any correspondence should be addressed.

⁶ Present address: 2nd Department of Neurosurgery, University of Athens Medical School, Attikon University Hospital, 1 Rimini Str., 12462 Athens, Greece.

Keywords: STN-DBS, Parkinson's disease, biomarkers, electrophysiological mapping techniques, stochastic dynamics

1. Introduction

Since its first application in 1993, high frequency deep brain stimulation (DBS) of the subthalamic nucleus (STN) has evolved into a reference surgical procedure for the treatment of levodopa-sensitive symptoms, in patients with advanced Parkinson's disease (PD) (Benabid *et al* 1994, Limousin *et al* 1995, Benabid *et al* 2009). Accurate electrode placement is, according to the surgical consensus, a critical factor in achieving the best clinical results and minimizing stimulation-induced side effects (Benabid 2003, Lozano *et al* 2010). To compensate for certain drawbacks related to preoperative stereotactic targeting (MRI distortion, brain shift and increased risk of complications in ventriculography), electrophysiological mapping techniques are encompassed in the neurosurgical procedure by the vast majority of medical centers (Abosch *et al* 2013, Lozano *et al* 2010). The principal mapping tools used are microelectrode recording (MER) of neuronal activity in the target area and intraoperative stimulation carried out through macrostimulation testing (Abosch *et al* 2013, Marceglia *et al* 2010).

The ultimate goal of MER techniques during STN-DBS surgery is ascertainment of the trajectory with the highest extension of typical STN activity (Marceglia *et al* 2010). An increased background noise level, a high discharge rate and an irregular or bursting pattern of activity are distinguishing features of the STN with respect to the surrounding brain structures (Bour *et al* 2010). Following delineation of the functional boundaries of the STN, its total length for each recording track can be defined. An acceptable track should pass through ≥ 3 mm of the nucleus (Marceglia *et al* 2010). Apart from the aforementioned criteria, intraoperative evaluation of macrostimulation-induced effects is a major contributory factor in the selection of the optimal trajectory (Schlaier *et al* 2013, Reck *et al* 2012). Typically, $60 \mu\text{s}$ pulses in trains of 130 Hz and a variable intensity up to a few milliamps are delivered through the low-impedance shaft of the microelectrode. The ratio between the intensity threshold for the appearance of side effects (motor contractions; oculomotor signs) and the intensity threshold for clinical effectiveness (most frequently involving rigidity improvement) defines the extent of the therapeutic window (Pollak *et al* 2002, Gross *et al* 2006, Marceglia *et al* 2010). By the end of electrophysiological mapping, comparative appraisal of the data acquired through both MER and macrostimulation, determines the selection of the optimal trajectory and the optimal site for implantation of the DBS electrode (Bour *et al* 2010, Reck *et al* 2012).

In the context of microelectrode mapping, methods aiming at enhanced objectivity and reduced operation time have been extensively investigated (Falkenberg *et al* 2006, Danish *et al* 2008, Zaidel *et al* 2009, Wong *et al* 2009, Novak *et al* 2011, Cagnan *et al* 2011, Pinzon-Morales *et al* 2011). In that respect, combinatorial application of quantitative features related to the local field potential (LFP) and/or the high-pass filtered signal (i.e. the high-frequency background activity or

the spiking activity) has been evaluated. Nevertheless, whereas multi-feature approaches provide increased accuracy and reliability for STN targeting, the use of a unique robust biomarker would substantially simplify and accelerate intraoperative nucleus detection. In addition to the aforementioned perspective, a complementary single-biomarker approach applicable to the process of intraoperative stimulation would lead to significant improvement of the entire electrophysiological procedure, by optimizing clinical decision making and decreasing total surgical time.

There is emerging evidence suggesting correlation of subthalamic oscillatory synchronization with clinical impairment in PD (Kühn *et al* 2009, Pogosyan *et al* 2010), and, conversely, desynchronization of the neuronal activity as a possible mechanism of action of STN-DBS (Carlson *et al* 2010, Walker *et al* 2011, Hauptmann *et al* 2007, Modolo and Beuter 2009, Wilson *et al* 2011, Johnson *et al* 2013). In light of this evidence, the main objective of this study was to evaluate collective dynamical and response properties of the subthalamic oscillatory activity as crucial hallmarks for the selection of the optimal stimulation site during DBS for PD. Specifically, we aimed to assess the applicability of two complementary single-biomarker approaches within the principal mapping techniques that are commonly used intraoperatively: MER and macrostimulation testing. Within this frame of reference, based upon MERs acquired during ten surgical interventions, we initially assessed a multivariate phase synchronization index (Carmeli *et al* 2005, Allefeld *et al* 2007, Polychronaki 2011) as a combined measure of local and spatially extended oscillatory synchronization (Moran and Bar-Gad 2010), keeping susceptibility to measurement noise to a minimum (Rossberg *et al* 2004, Sun *et al* 2008). Implementation of the proposed index was intended to point to the acceptable trajectories, i.e. the trajectories that would be the best candidates for macrostimulation (Marceglia *et al* 2010). This feature was subsequently employed as one of the constituent parameters of a stochastic phase model appropriately fitted to pre-selected MERs. Based on this model, we assessed the Lyapunov exponent (Pikovsky *et al* 2001) as a quantity reflecting subthalamic synchronization dynamics in response to periodic inputs (130 Hz) and further evaluated its predictability in identification of the sites where stimulation yielded the best clinical benefit. The entire automatic methodology was evaluated based on the decisions made intraoperatively by clinical experts.

2. Patients and methods

2.1. Patients and surgery

During a one-year period, ten patients underwent implantation of DBS electrodes in the STN, at the Department of Neurosurgery at Evangelismos General Hospital of Athens. Three women and seven men participated with informed consent and the permission of the local ethics committee. Their ages

Table 1. Presentation of patients' clinical details.

Case	Age (years) and sex	Disease duration (years)	Hemisphere(s) tested	Motor UPDRS on/off drugs pre-op	Motor UPDRS on/off drugs post-op	Lev. equiv. pre-op/post-op	Site with the best therapeutic window ^a	Clinical outcome
1	59, f	11	Right STN/ left STN	12/40	14/38	850/750	C 0/A -0.5	Moderate
2	53, f	16	Right STN	16/52	8/18	1450/600	A -1.0	Excellent
3	66, m	19	Left STN	28/72	24/62	1000/600	P -2.0	Moderate
4	53, m	10	Right STN/ left STN	16/53	18/24	1100/300	P 0/L -2.0	Excellent
5	62, m	18	Right STN/ left STN	23/68	18/38	1400/500	M -1.0/P 0	Excellent
6	50, m	16	Right STN	26/66	24/28	1400/450	P 0/C 0	Excellent
7	70, m	13	Right STN	24/58	20/34	750/450	C -1.0	Excellent
8	62, m	15	Right STN/ left STN	32/70	30/41	1800/750	P -1.0/P +1.0	Excellent
9	64, m	14	Right STN	28/75	22/32	1600/600	L -1.5	Excellent
10	67, f	13	Left STN	24/61	26/54	1150/850	M -1.0	Moderate

m, male; f, female; pre-op, preoperatively; post-op, postoperatively; C, central; L, lateral; A, anterior; P, posterior; M, medial.

^a mm above anatomical target point (0 mm); +, mm below anatomical target point (0 mm).

ranged from 50 to 70 years, with a mean of 60 years. The clinical criteria included idiopathic PD (as documented by a positive response to levodopa) with motor fluctuations and/or dyskinesias. The mean disease duration was 14.5 years (range: 10–19 years). The mean motor Unified Parkinson's Disease Rating Scale (UPDRS) score preoperatively in the off-medication state was 61.5 (range: 40–75) and 22.9 (range: 12–32) in the on-medication state. Anti-parkinsonian medication was withdrawn at least 12 hours before surgery. Table 1 summarizes patient clinical characteristics.

Stereotactic surgery was based on pre-operative anatomical targeting of the STN, MER and high frequency test stimulation (Sakas *et al* 2007, Boviatsis *et al* 2010). Patients underwent application of a CRW stereotactic frame (Cosman–Roberts–Wells; Radionics, Burlington, MA, USA) under local anesthesia and in a way that the anterior commissure/posterior commissure (AC-PC) plane was approximately parallel to the base plane of the frame. Anatomical targeting of the STN was achieved via both indirect visualization according to a stereotactic atlas (Schaltenbrand and Wahren 1977) and direct visualization according to an image fusion technique. This technique involved a combination of frameless T2-weighted magnetic resonance imaging (MRI) and framebased computed tomography (CT) and was developed on a Radionics hardware/software system (StereoPlan; Integra Radionics, Burlington, MA, USA). The coordinates obtained with both indirect and direct methods were combined for determination of the anatomical target point used during microelectrode mapping. The surgical procedure was performed under local anesthesia. Fourteen mm diameter, burr holes were centered over a point anterior to the coronal suture and 3.4 cm lateral to midline. Stereotactic arc settings ranged from 55° to 70° for declination, and slide settings were 10°–15°. Microelectrodes were placed on a five-channel holder with central, lateral, medial, anterior and posterior positions, 2 mm apart (Ben's gun). The initial point of MER was typically within the white matter, superior and rostral to the thalamic reticular shell. A micropositioner

(Microtargeting Drive; Medtronic, Minneapolis, MN) was used to advance the microelectrode in submillimeter steps. At each site, signals were recorded for ≤10 s. Visual and auditory analyses were performed on-line by two clinical experts. The electrophysiological criteria used to distinguish the STN were an increased background noise level and neuronal responses to passive movements of the patients' extremities. At the end of MER mapping, the total penetrated length of the STN was noted for each recording track. Following determination of the trajectories traversing the broadest extent of the nucleus, macrostimulation was performed usually at three selected depth positions with an external pulse generator (Medtronic Screener Model 3625; Medtronic, Minneapolis, MN). The stimulation parameters utilized were a frequency of 130 Hz, a pulse width of 60 μs and amplitudes up to 5 V. Rigidity improvement was judged on passive movements of the contralateral wrist, whereas the assessment of side effects was mainly based on observation of certain motor contractions and/or of tonic eye deviation and/or blurred vision. Once the site with the best therapeutic window was identified, the DBS lead (Medtronic electrodes 3389 and 3387) was advanced 2 mm, in order for the contacts to 'encompass' the optimal target point, and finally anchored with a Navigus cap (Image Guided Neurologics, FL, USA). Final lead placement was confirmed with fluoroscopy. The same procedure was then repeated for the other side, in cases of bilateral surgery. Post-operative MRI was performed within two days to confirm the location of the DBS electrodes before they were connected to the internal pulse generator (IPG) (Kinetra; Medtronic, Minneapolis, MN).

2.2. Data description

A commercially available microrecording system (Leadpoint TM Neural Activity Monitoring System; Medtronic, Minneapolis, MN) was used to acquire and store data. Five 60 μm tungsten tip microelectrodes (Medtronic, Minneapolis, MN)

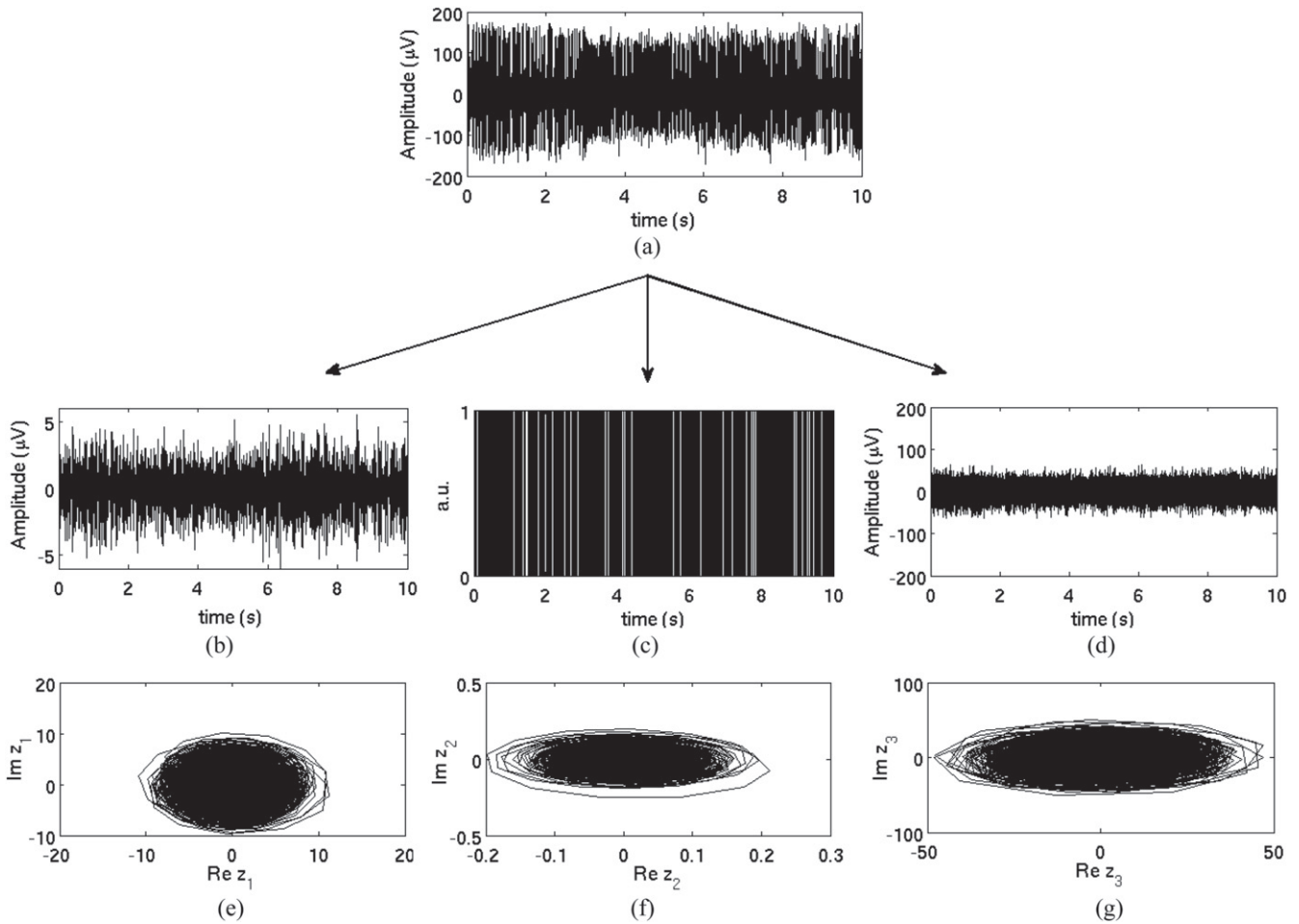


Figure 1. Multi-scale neuronal activity and optimal filtering. (a) Example of a raw extracellular signal recorded in the right STN, case 2 (recording site depth: A +0.5). (b)–(d) The three derived signals: LFPs, spiking activity (a.u. = arbitrary units) and background unit activity, respectively. (e)–(g) The trajectories of the filtered signals $z(t)$ (see section 2.4.2) obtained from series (b)–(d), respectively, after low-frequency amplitude modulation (of series (c) and (d)) and down-sampling to 1 kHz.

were used for recording. The recorded signal was pre-amplified, band-pass filtered between 0.1 Hz and 10 kHz and 1000× amplified (Nicolet Viking IV; Nicolet Biomedical, Madison, USA). The signal was sampled at 24 kHz using a 16-bit A/D converter (CED Power1401; Cambridge Electronic Design, Cambridge, UK). In total, data from 70 MER trajectories obtained from ten STN-DBS procedures were retrospectively analyzed in Matlab (Mathworks, Natick, MA), (table 1). Initially, the acquired signals were digitally band-pass filtered at 1–141 Hz and 0.5–10 kHz applying four-pole Butterworth filters.

2.3. Signal preprocessing

The extracellular signal recorded from the microelectrode (figure 1(a)) conveys the sum of two complementary signals acquired by the aforementioned frequency-band separation: the multi-unit activity reflected in the high frequency signal component and the LFPs reflected in the low-frequency signal component (Logothetis 2002). The LFPs predominantly represent synaptic events in a neural population within a large radius (0.5–3 mm) of the electrode tip (Mitzdorf 1987). By

contrast, the multi-unit activity reflects the spiking activity of a neural population within a small radius (200–300 μm) of the electrode tip (Logothetis 2002). The multi-unit activity actually consists of spiking activity of one or just a few large isolated cells and background unit activity, which represents the sub-noise level spiking activity of the surrounding neural population (Moran and Bar-Gad 2010).

Accordingly, the methods we present here were based on the assessment of multi-scale neuronal activity: (a). spiking activity quantified through the spike detection process, (b). activity of small neural populations quantified through the background unit activity extraction process (Moran *et al* 2008), and (c). activity of large neural populations reflected in the LFPs (figures 1(b)–(d)).

2.3.1. Mechanical artifacts—extraction of spiking and background unit activity. Occasional events, like vibrational effects, 50/60 Hz power-line interference and static discharge may result in high amplitude artifacts (Dolan *et al* 2009). Automatic detection and elimination of high amplitude artifacts was based on noise level estimation, as proposed by Dolan *et al* (2009). Low amplitude artifacts were also

detected and excluded from further analysis as described by Cagnan *et al* (2011).

The spike detection process involved application of morphological criteria based on a five-point spike template (Wong *et al* 2009, Cagnan *et al* 2011). Specifically, we employed an amplitude threshold set at 3.5 times the estimated noise level, and hard-coded thresholds for the peak-to-peak spike width and the distance between zero crossings flanking the candidate spike.

Reconstruction of the background unit activity (figure 1(d)) was performed eliminating the bias of dominant spikes (Moran *et al* 2008). Thus, following identification of the spiking activity, the surrounding time windows (−0.5 to +2.5 ms around the spike identification point) were removed and the empty segments were replaced by randomly chosen 3 ms spike-free windows from the same recorded trace. Small inconsistencies between the real and the inserted spike-free segments were considered negligible for power alterations in the low-frequency range (Moran and Bar-Gad 2010).

2.4. MER—automatic detection of STN borders and identification of acceptable trajectories

For automatic delineation of the functional boundaries of the STN during MER based on a single-biomarker approach, we quantified and integrated dynamic interactions between pairs of the three distinct signals: (1) the spiking activity, (2) the background unit activity, and (3) the LFPs (figures 1(b)–(d)). To this end, we performed phase synchronization analysis (Tass *et al* 1998, Carmeli *et al* 2005, Allefeld *et al* 2007, Polychronaki 2011), restricted to the beta frequency band, in light of strong evidence that beta oscillatory synchronization in the STN is dramatically increased in the pathological state (Kühn *et al* 2005, Weinberger *et al* 2006, Moran and Bar-Gad 2010).

2.4.1. Envelope extraction. Importantly, in addition to the LFPs, the envelope of the high-frequency signal component may also yield power in the low-frequency range (1–141 Hz) (Logothetis 2002, Moran and Bar-Gad 2010). In that respect, the low-frequency envelope of the background unit activity signal was extracted employing the full-wave rectification (FWR) method, before a four-pole Butterworth filter was applied (passband 1–141 Hz). This filter was also used in order to recover the low-frequency amplitude modulation of the spiking activity. All signals were further down-sampled to 1 kHz.

2.4.2. Data-driven optimal filtering. On account of the presence of measurement noise (Hurtado *et al* 2004, Rossberg *et al* 2004, Sun *et al* 2008), a complex-valued, linear bandpass filter was applied, prior to the phase reconstruction procedure as described by Rossberg *et al* (2004). In particular, optimization was performed under the constraint of a spectral window ranging within 10–33 Hz, taking into consideration that beta band activity may also be expressed at frequencies below 13 Hz or above 33 Hz (Tsirogiannis *et al* 2010). Exemplary trajectories of the

filtered signals ($z(t)$) corresponding to the multi-scale neuronal activity are illustrated in figures 1(e)–(g).

2.4.3. Instantaneous phase reconstruction. In order to maximize reliability in the detection of phase synchronization, phase evolution ϕ was obtained from the complex magnitude of the filtered signal ($z(t)$) by means of the method of neighborhood-based phase estimation (NPE) proposed by Sun *et al* (2008). Adoption of this method was motivated by its improved efficacy over application of the Hilbert transform (figure 2(b)). The principle of NPE is based on Takens' theorem (Takens 1981) and on the fact that in the phase space reconstructed by time-delay embedding, the state recurrences of a reference vector are represented by its nearest neighbors. Selection of embedding dimension d and number of neighbors N (figure 2(a)) is discussed in section 2.4.6.

2.4.4. Bivariate phase synchronization index. We employed as a measure for bivariate phase synchronization an index based on the Shannon entropy (Tass *et al* 1998), detailed in appendix A.

Eventually, at each recording site along a specific trajectory, a set of synchronization index time series $\rho_{1,2}(t)$, $\rho_{1,3}(t)$ and $\rho_{2,3}(t)$ corresponding to the pairs of the oscillatory signals (spiking activity—background unit activity, spiking activity—LFPs and background unit activity—LFPs) was assessed and their mean amplitudes $\rho_{1,2}$, $\rho_{1,3}$, $\rho_{2,3}$ were retrieved (figures 3(e)–(g)).

2.4.5. STN detection and determination of acceptable MER trajectories. For delineation of the STN borders based on a robust single biomarker, we used a multivariate phase synchronization measure (figure 3(h)) as a means to quantify dynamic interactions between the three scales ($K=3$) of neuronal populations (Carmeli *et al* 2005) given by

$$Q = 1 + \frac{\sum_{i=1}^K \lambda'_i \log \lambda'_i}{\log(K)}, \quad (1)$$

where λ'_i are the normalized eigenvalues ($\lambda'_i = \frac{\lambda_i}{K}$) belonging to the $K \times K$ matrix of bivariate phase synchronization indices (Allefeld *et al* 2007, Polychronaki 2011). In particular, eigenvalue decomposition was applied on the following matrix:

$$P = \begin{bmatrix} 1 & \rho_{1,2} & \rho_{1,3} \\ \rho_{1,2} & 1 & \rho_{2,3} \\ \rho_{1,3} & \rho_{2,3} & 1 \end{bmatrix}. \quad (2)$$

A MER trajectory was considered acceptable if there existed a distance ≥ 3 mm (Marceglia *et al* 2010) along which Q remained above the synchronization index threshold Q_{thres} (evaluation of Q_{thres} is described in the next paragraph). The first site (located dorsally) along that distance was defined as the dorsal border of the STN, whereas the last site (located ventrally) was defined as the ventral border of the STN. The

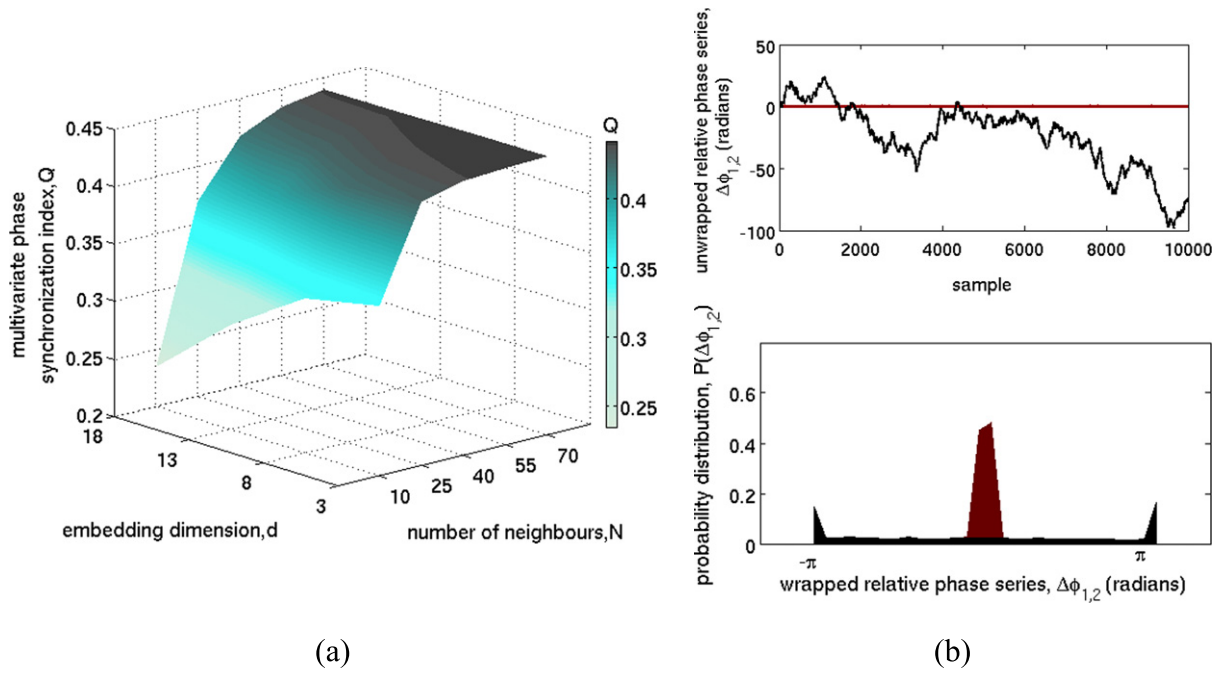


Figure 2. Selection of optimal parameters for the NPE method and reconstruction of the relative phase series. (a) Mean value of synchronization index Q within the STN boundaries for a range of combinations of embedding dimension d and number of neighbors N , averaged over 21 MER trajectories to which a positive detection was ascribed by the clinical experts. (b) The top panel shows the unwrapped relative phase series $\Delta\phi_{1,2}$, corresponding to the pair of the oscillatory signals presented in figures 1(c)–(d). The red line indicates the result obtained based on combinatorial application of data-driven optimal filtering and the NPE method. The black line indicates the result that would be obtained, in case a traditional linear band-pass filter in combination with the Hilbert transform were applied. In the lower panel, the respective distributions $P(\Delta\phi_{1,2})$ of the wrapped relative phase series are depicted.

detection process described is evaluated in section 3 with respect to its efficacy to point to acceptable MER trajectories that are likely to be further considered during macrostimulation testing.

2.4.6. Optimal embedding parameters and threshold calculation. In order to determine the optimal embedding dimension and number of nearest neighbors for the NPE method, we examined how the mean value of synchronization index Q within the STN boundaries evolved as a function of these parameters, in a total of 21 trajectories defined as acceptable by the clinical experts (figure 2(a)). Results showed that Q increased very slowly after N had reached particular values ($40 \leq N \leq 50$) even for small values of embedding dimension ($d=3$). On the other hand, over-embedding ($d > 11$) reduced markedly the performance of the method. We set $N=70$ and $d=3$, since these values yielded the maximal estimate of synchronization index Q .

Synchronization index threshold Q_{thres} was determined by optimizing the performance of the STN-detection method with respect to the annotations made intraoperatively. Specifically, Q_{thres} was defined as the maximum threshold whose application minimized the false negative and false positive rates in the 70—MER—trajectories data set ($Q_{\text{thres}} = 0.37$).

2.5. Macrostimulation—automatic assessment of the sites related to the most beneficial clinical response

Automatic determination of the sites where intraoperative test macrostimulation conferred greater clinical effectiveness was based on increasing evidence that the beneficial effects of STN-DBS are mediated by modification of the abnormal firing pattern in the STN and disruption of neural population synchrony (Carlson *et al* 2010, Walker *et al* 2011, Hauptmann *et al* 2007, Modolo and Beuter 2009, Wilson *et al* 2011, Johnson *et al* 2013). Thereupon, employing a stochastic phase model and using the multivariate phase synchronization index Q as one of its constituent parameters, we simulated the neuronal response to macrostimulation at selected recording sites. This response could be quantified by means of a distinct single biomarker, the Lyapunov exponent. In the context of nonlinear dynamics, the Lyapunov exponent characterizes the convergence/divergence properties of two nearby trajectories in the phase space (Pikovsky *et al* 2001). Positive values of the Lyapunov exponent indicate desynchronization. Based on the aforementioned facts, we examined the Lyapunov exponent as an implicit indicator of the clinical effectiveness of stimulation during DBS surgery.

2.5.1. The phase model. We consider the following Langevin equation (by virtue of the Stratonovich

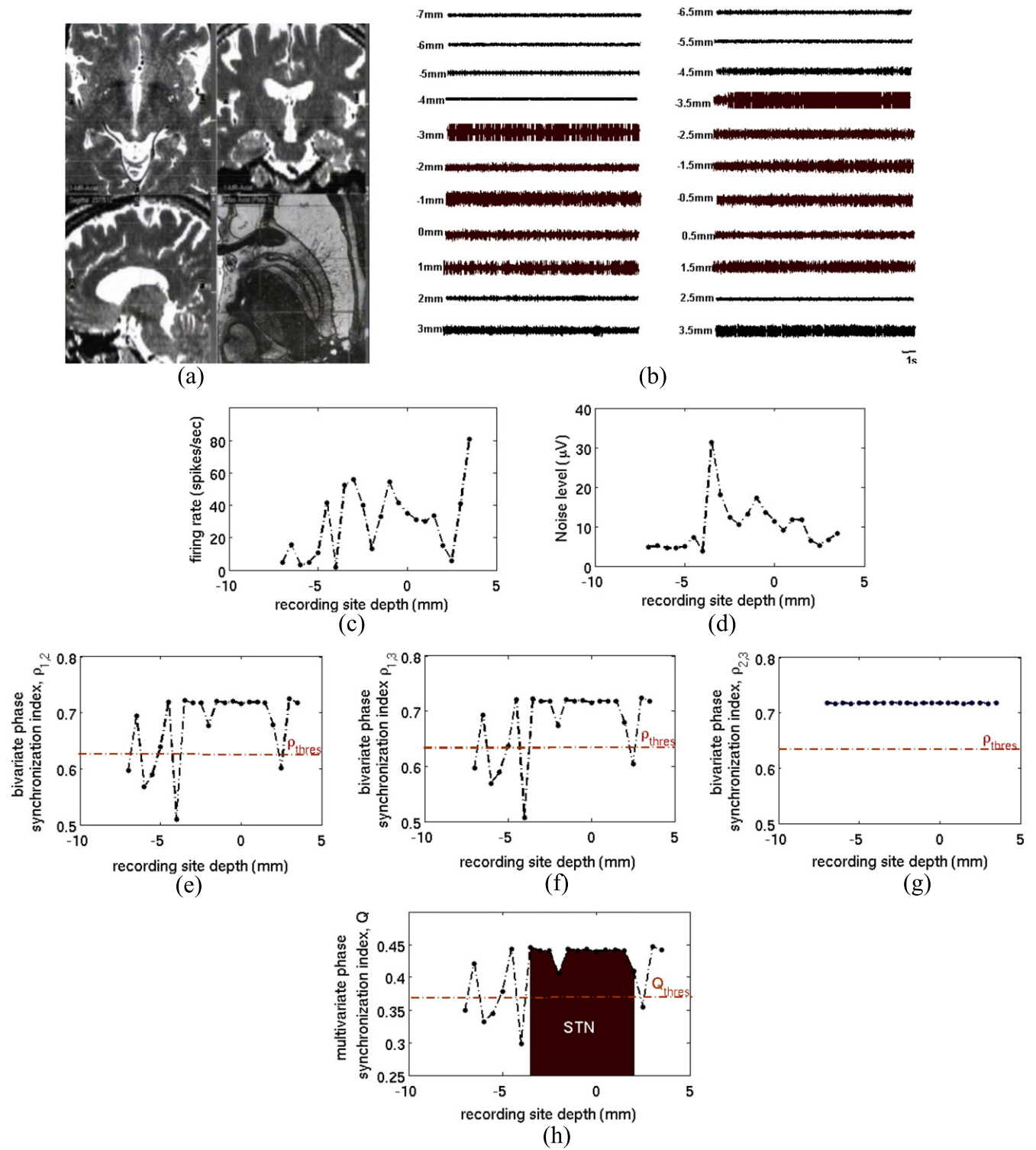


Figure 3. Assessment of the multivariate phase synchronization index Q along the lateral trajectory in the right hemisphere of case 1. (a) Planning of the target based on the image fusion hardware system (StereoPlan; Integra Radionics, Burlington, MA, USA). (b) 10 s MER epochs obtained in sub-millimeter steps. Depth value 0 corresponds to the anatomical target point determined preoperatively. (c)–(d) Respective changes in firing rate and noise level. (e)–(g) The mean amplitudes $\rho_{1,2}$, $\rho_{1,3}$ and $\rho_{2,3}$ of the bivariate phase synchronization indices as a function of the recording site depth. (h) The multivariate phase synchronization index Q . The dashed horizontal line indicates the generic threshold $Q_{\text{thres}} = 0.37$. The dark region corresponds to the STN length determined intraoperatively by the clinical experts.

interpretation (Gardiner 1985)) describing an ensemble of N globally coupled identical phase oscillators, driven by intrinsic independent and extrinsic common noises, but also subject to periodic forcing:

$$\frac{d\phi_i}{dt} = \omega + \frac{K}{N} \sum_{j=1}^N \sin\left(2\pi(\phi_j - \phi_i)\right) + \sigma_I R_I(\phi_i) \xi_i(t) + \sigma_C R_C(\phi_i) \eta(t) + \Delta(\phi_i, \beta) \sum_k \delta(t - kT_s). \quad (3)$$

Here $\phi_i \in [0,1)$ is the phase variable of the i th oscillator, ω is its natural frequency and $K > 0$ is the coupling strength. We assume that $\xi_i(t)$ is zero mean Gaussian white noise, added independently to each oscillator, with correlation specified by $\langle \xi_i(t) \xi_j(t') \rangle = \delta_{ij} \delta(t - t')$, where $\delta_{ij} = 1$ if $i = j$ and 0 if $i \neq j$. We regard $\eta(t)$ as colored noise with zero mean and unitary variance, i.e. with autocorrelation function $C(t) = \langle \eta(t) \eta(0) \rangle = \frac{1}{2\tau_C} e^{-\frac{|t|}{\tau_C}}$. Thus, $\eta(t)$ can be regarded as an Ornstein–Uhlenbeck process with correlation time τ_C (Gardiner 1985). σ_I and σ_C are small parameters representing the intensity of independent and common noise, respectively. $R_C(\phi_i)$ and $R_I(\phi_i)$ are phase sensitivity functions that represent the linear response of the phase variable ϕ_i to the respective infinitesimal noise perturbations, while $\Delta(\phi_i, \beta)$ is the phase response curve (PRC) to a single (DBS) impulse (Kuramoto 1984, Winfree 2001) (see appendix B). β represents the stimulus amplitude (see appendix B), $T_s = 130\text{Hz}$ is the period of the stimulation and $0 \leq k < \infty$.

Introducing the (complex) Kuramoto order parameter defined by $re^{2\pi i\psi} = \frac{1}{N} \sum_{j=1}^N e^{2\pi i\phi_j}$ (Kuramoto 1984), (3) can be rewritten as (Strogatz 2000):

$$\frac{d\phi}{dt} = \omega + Kr \sin(2\pi(\psi - \phi)) + \sigma_I R_I(\phi) \xi(t) + \sigma_C R_C(\phi) \eta(t) + \Delta(\phi, \beta) \sum_k \delta(t - kT_s), \quad (4)$$

where r characterizes the degree of synchrony and ψ is the mean phase of the oscillators. Next, defining the effective drift and diffusion coefficients (Nakao *et al* 2010)

$$v = \sigma_C^2 \int_0^\infty ds C(s) \int_0^1 d\phi R'_C(\phi) R_C(\phi - \omega s) \\ D = \sigma_C^2 \int_{-\infty}^\infty ds C(s) \int_0^1 d\phi R_C(\phi) R_C(\phi - \omega s) \quad (5)$$

we obtain the following white-noise Langevin equation:

$$\frac{d\phi}{dt} = \omega + Kr(\sin 2\pi(\psi - \phi)) + \sigma_I R_I(\phi) \xi(t) + v + \sqrt{D} \xi(t) + \Delta(\phi, \beta) \sum_k \delta(t - kT_s) \quad (6)$$

or

$$\frac{d\phi}{dt} = \omega + Kr \sin(2\pi(\psi - \phi)) + v + (\sigma_I R_I(\phi) + \sqrt{D}) \times \xi(t) + \Delta(\phi, \beta) \sum_k \delta(t - kT_s). \quad (7)$$

The Stratonovich equation (7) is converted to an equivalent Ito stochastic differential equation (Gardiner 1985):

$$\frac{d\phi}{dt} = \omega + Kr \sin(2\pi(\psi - \phi)) + v + (\sigma_I R_I(\phi) + \sqrt{D}) \times \xi(t) + \frac{\sigma_I}{2} R'_I(\phi) (\sigma_I R_I(\phi) + \sqrt{D}) + \Delta(\phi, \beta) \sum_k \delta(t - kT_s). \quad (8)$$

Phase equation (8) is solved through the stochastic map from one stimulus cycle to the next (Nesse and Clark 2010). The phase dynamics during the inter-impulse interval T_s is described by

$$\phi_{n+1} = \phi_n + (\omega + Kr \sin(2\pi(\psi - \phi_n)) + v + \frac{\sigma_I}{2} R'_I(\phi_n) (\sigma_I R_I(\phi_n) + \sqrt{D})) T_s + (\sigma_I R_I(\phi_n) + \sqrt{D}) W(T_s) + \Delta(\phi_n, \beta), \quad (9)$$

where $W(t)$ is a Wiener process with probability density function f_W , which is a Gaussian with zero mean and variance T_s . The stochastic map is defined by the (‘modulo-one’) Perron–Frobenius operator F , that maps the density of phases at the time of the $(n + 1)$ th impulse, $p_{n+1}(\phi)$, onto the density of phases at the time of the n th impulse, $p_n(\phi)$ (Ermentrout and Saunders 2006, Nesse *et al* 2007, Yamanobe and Pakdaman 2002):

$$p_{n+1}(\phi) = \int_0^1 \sum_{j \in \mathbb{Z}} f_W \left(\frac{\phi - \phi' + j - \left(\omega + Kr \sin(2\pi(\psi - \phi')) + v + \frac{\sigma_I}{2} R'_I(\phi') (\sigma_I R_I(\phi') + \sqrt{D}) \right) \times T_s - \Delta(\phi', \beta)}{(\sigma_I R_I(\phi') + \sqrt{D})} \right) \frac{1}{(\sigma_I R_I(\phi') + \sqrt{D})} p_n(\phi') d\phi'. \quad (10)$$

Setting

$$A(\phi, \phi')$$

$$= \sum_{j \in Z} f_{W_j} \left(\begin{array}{c} \phi - \phi' + j \\ \left(\omega + Kr \sin(2\pi(\psi - \phi')) + v \right) \\ - \left(\frac{\sigma_I}{2} R'_I(\phi') (\sigma_I R_I(\phi') + \sqrt{D}) \right) \\ \times T_s - \Delta(\phi', \beta) \\ \left(\sigma_I R_I(\phi') + \sqrt{D} \right) \end{array} \right) \cdot \frac{1}{\left(\sigma_I R_I(\phi') + \sqrt{D} \right)} \quad (11)$$

and discretizing the density into $M=500$ bins of size $1/M$, we obtain:

$$\int_0^1 A(\phi, \phi') p(\phi') d\phi' \approx \frac{1}{M} \sum_{j=0}^{M-1} A\left(\frac{i}{M}, \frac{j}{M}\right) p^j. \quad (12)$$

Hence, the stochastic map is approximated using a 500×500 transition matrix (stochastic kernel) having all positive entries and a spectral radius of 1 (figure 4). This matrix possessed the strong Perron–Frobenius property (Noutsos and Tsatsomeros 2008). The iterated mapping (10) converges to the steady-state phase distribution (invariant density) after h number of stimuli:

$$p_{st}(\phi) = \left[F^h p_0 \right](\phi). \quad (13)$$

This distribution is represented by the eigenvector corresponding to the dominant (unit) eigenvalue of A (figures 4(j)–(l)). To quantify the stability of the synchronized states we calculate the Lyapunov exponent (figure 5), using phase map (9), as (Pikovsky *et al* 2001, Teramae and Tanaka 2004):

$$\begin{aligned} \lambda &= \frac{\left\langle \ln \left| \frac{d\phi_{n+1}}{d\phi_n} \right| \right\rangle}{T_s} \\ &= \frac{1}{T_s} \left\langle \ln \left| 1 + \left(-2\pi Kr \cos(2\pi(\psi - \phi)) + \frac{\sigma_I}{2} R''(\phi) \right) \right. \right. \\ &\quad \left. \left(\sigma_I R_I(\phi) + \sqrt{D} \right) + \frac{\sigma_I^2}{2} (R'_I(\phi))^2 \right) T_s \\ &\quad \left. + \left(\sigma_I R_I(\phi) + \sqrt{D} \right) W(T_s) + \Delta'(\phi, \beta) \right|_{W(T_s)} \right\rangle \\ &= \frac{1}{T_s} \int_0^1 d\phi \ln \left| 1 + \left(-2\pi Kr \cos(2\pi(\psi - \phi)) \right. \right. \\ &\quad \left. \left. + \frac{\sigma_I}{2} R''(\phi) (\sigma_I R_I(\phi) + \sqrt{D}) \right) \right) T_s \\ &\quad \left. + \Delta'(\phi, \beta) \right| \cdot p_{st}(\phi). \end{aligned} \quad (14)$$

2.5.2. Determination of model parameters. For each depth position selected for macrostimulation, there are eight parameters that must be estimated in the phase model (8): ω , r , K , ψ , σ_C , v , D and σ_I . We set $\omega = 1$ according to Wilson

et al (2011). We also consider $\psi = 0$. The remaining parameters are estimated on the basis of the respective signal acquired during MER, which is considered to reflect a no-input stimulus epoch (figure 6).

The modulus r of the order parameter is set equal to the value of the phase synchronization index Q , estimated in section 2.4.5. Coupling strength K is estimated by (Allefeld and Kurths 2004, Allefeld *et al* 2007):

$$K = \lambda \mu^2, \quad (15)$$

where $\lambda > 1$ is the largest eigenvalue of matrix (2) and μ is the first element of the corresponding eigenvector.

As indicated by (5), calculation of parameters v and D is dependent on estimation of σ_C and $C(t)$. The intensity of common noise σ_C is determined through evaluation of the power spectral density function of the background unit activity (Moran and Bar-Gad 2010) using Welch’s method, while the autocorrelation function of this signal is used as an estimate of $C(t)$.

Once the above parameters were estimated, we proceed to evaluate the intensity of independent noise σ_I , through definition of the first passage time problem for the phase model (8) with no input (see appendix C).

2.6. Performance evaluation

To assess the performance of the entire automatic methodology, the dataset of the decisions made intraoperatively by two clinical experts (PGS and GAT) was used as the gold standard.

Significant changes in the multivariate phase synchronization index within the intraoperatively determined STN length were evaluated by applying a two-sample t -test (statistical significance was defined at $p < 0.05$). Additionally, stability of the phase synchronization indices in the presence of measurement noise was assessed and compared with the stability of firing rate and noise level measures within the STN boundaries. Comparative assessment was based on evaluation of the standard deviation of the corresponding normalized measures (two-sample t -test, $p < 0.05$). Normalization was performed by dividing each measure by its mean value within the intraoperatively determined STN length. We finally proceeded to comparative assessment of the number of trajectories traversing the STN according to the automatic method and the clinical experts and determined the sensitivity of the method in detecting the dorsal and ventral borders of the STN.

Performance of the stochastic dynamical model for designation of the sites where stimulation yielded the best clinical benefit was assessed evaluating the sensitivity of the corresponding method under two principal conditions (two-sample t -test, $p < 0.05$).

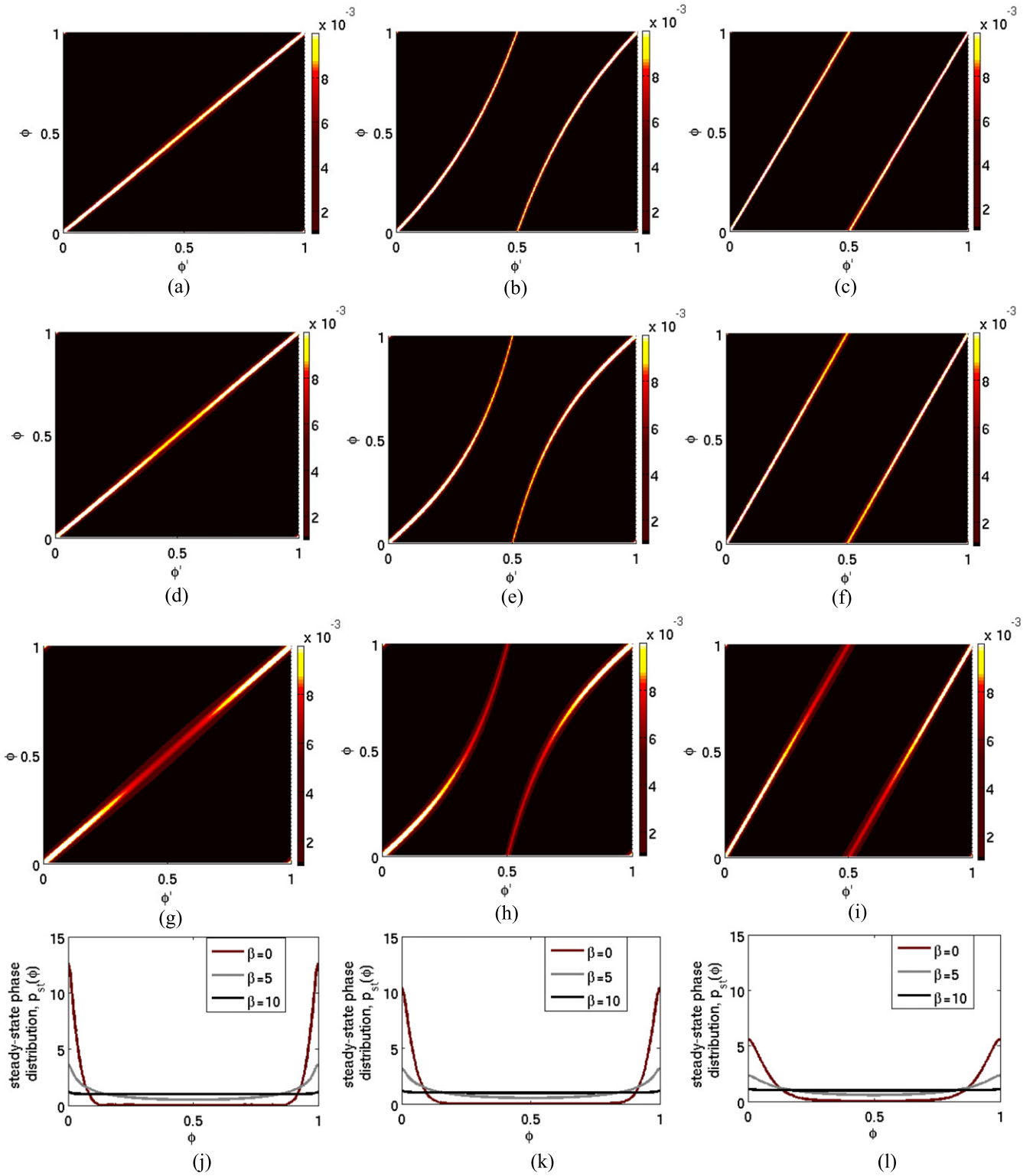


Figure 4. (a)–(i) Stochastic kernel functions $A(\phi, \phi')$ based on MERs at: (a)–(c) C 0, right STN, case 1, for $\beta=0, \beta=5$ and $\beta=10$, respectively, (d)–(f) P +2, right STN, case 5, for $\beta=0, \beta=5$ and $\beta=10$, respectively and (g)–(i) P +2, right STN, case 6, for $\beta=0, \beta=5$ and $\beta=10$, respectively. (j)–(l) Steady-state phase distributions for $\beta = 0$ (red line), $\beta = 5$ (gray line) and $\beta = 10$ (black line), corresponding to the cases described in (a)–(c), (d)–(f) and (g)–(i).

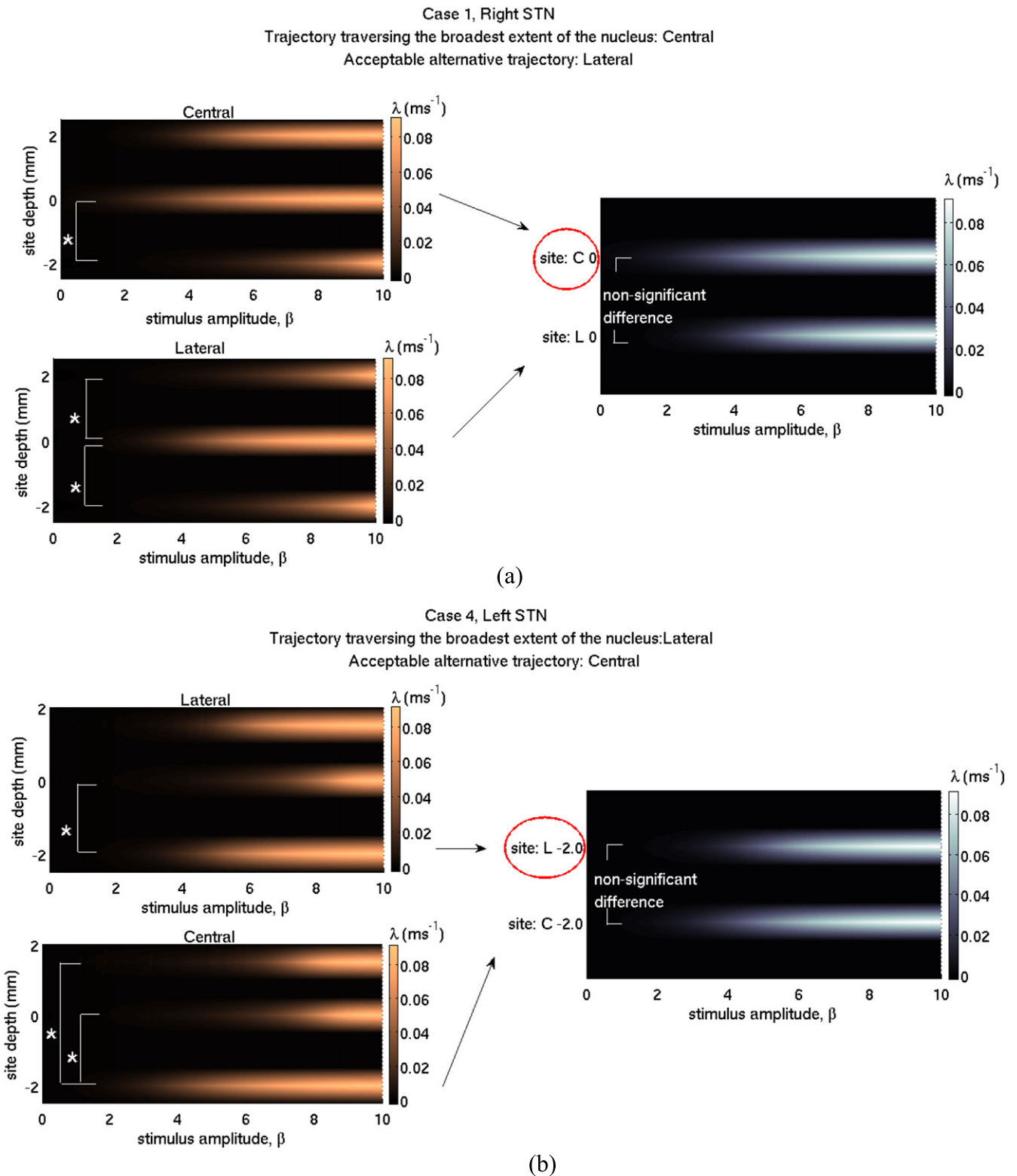


Figure 5. The Lyapunov exponent, λ as a function of stimulus amplitude β for a pair of acceptable trajectories in two distinct cases. (a) Left panels: the Lyapunov exponent, λ at three pre-selected sites of central (upper) and lateral (lower) trajectory, right hemisphere, case 1. Asterisks denote significant differences. Right panel: sites where the highest values of λ were obtained for each of the acceptable trajectories. At these sites, values of λ between the two trajectories were not significantly different. Circled is the optimal target point according to clinical decision. (b) Left panels: the Lyapunov exponent, λ at three pre-selected sites of lateral (upper) and central (lower) trajectory, left hemisphere, case 4. Right panel: sites where the highest values of λ were obtained for each of the acceptable trajectories. At these sites, values of λ between the two trajectories were not significantly different. Circled is the optimal target point according to clinical decision.

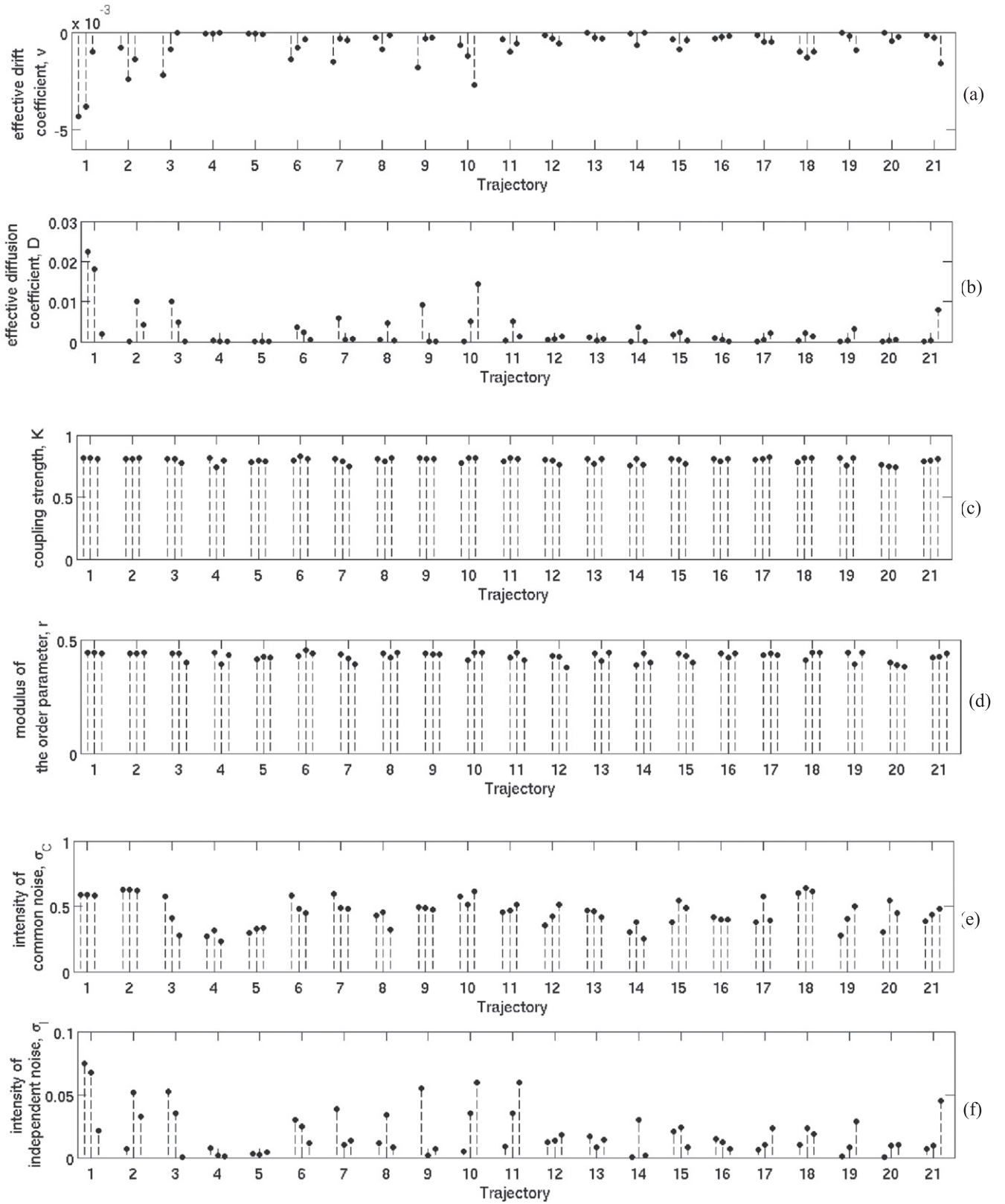


Figure 6. Parameter values based on MERs along 21 trajectories selected for macrostimulation testing by the clinical experts. For each trajectory, parameters are assessed at three site depths selected for intraoperative macrostimulation. Parameters depicted are (a) effective drift coefficient, v , (b) effective diffusion coefficient, D , (c) coupling strength, K , (d) modulus of the order parameter, r , (e) intensity of common noise, σ_c , and (f) intensity of independent noise, σ_i .

3. Results

3.1. Determination of acceptable MER trajectories

According to the annotations made intraoperatively by the clinical experts, 40 out of 70 trajectories penetrated a subthalamic dorsoventral extent greater than 3 mm. With reference to these positive detections Q displayed significantly higher average values within the STN compared to its average values within neighboring structures ($p = 10^{-11}$). Figure 3 displays an application example of the STN detection methodology, i.e. on the lateral trajectory, in the right STN of case 1. Importantly, there is a striking difference between the stability of firing rate and noise level values and the stability of phase synchronization index Q , observed within the STN. This result provides an indication for the robustness of phase synchronization index despite the presence of measurement noise. Overall, multivariate phase synchronization index Q displayed significantly higher stability within the STN compared with firing rate ($p = 10^{-17}$) and noise level measures ($p = 10^{-18}$) (figure 7).

Principally, the STN detection methodology demonstrated a false negative rate (FNR) of 4.8% and a false positive rate (FPR) of 0%. With reference to the true positive detections, the mean depth of the STN dorsal border according to the automatic algorithm was 0.0357 ± 0.1336 mm above the STN entry designated by the clinical experts. The mean depth of the STN ventral border was 0.0714 ± 0.3852 mm above the STN exit determined intraoperatively. Using a precision criterion of 0.5 mm within the current gold standard, the STN detection methodology yielded sensitivities of 100% and 92% for the STN dorsal and ventral border, respectively (table 2).

Interestingly, performance of the STN detection methodology based on the bivariate phase synchronization indices $\rho_{1,2}$ and $\rho_{1,3}$, was identical to the one based on synchronization index Q (table 2). However, it should be pointed out that the specific value of the multivariate synchronization index Q lied in its particular utility as a model parameter (section 2.5.2).

On the other hand, phase synchronization index $\rho_{2,3}$ displayed no discriminating power, as its average values within the STN were not significantly different from the average values outside the STN ($p = 0.9893$). This observation may reflect the fact that there exists a sparse correlation within the surrounding neural population not only within but also across the STN boundaries (Moran and Bar-Gad 2010).

3.2. Predictability of the Lyapunov exponent of the stochastic model in identification of the sites where stimulation yielded the best clinical benefit

Figure 4 depicts the stochastic kernel functions and invariant densities (obtained using (12)) for different values of stimulus amplitude β , derived based on MERs at three distinct site depths assessed for intraoperative macrostimulation. For $\beta = 0$, the proposed phase model reproduces the pathological synchronized state ($\phi = \phi'$), which appears to be more intense

in case 1 than in cases 5 and 6. With increasing β , the obtained states become gradually less synchronized in all cases. This observation was general across all site depths examined and strongly suggested that the desynchronizing effect of periodic stimulation was captured and validated by the current model. Figure 6 depicts a set of parameter values, derived based on 21 MER trajectories considered appropriate for macrostimulation testing by the clinical experts. We make the following observations: first and foremost, effective drift coefficient ν was always negative, as indicated by Nakao *et al* (2010). Secondly, coupling strength K was positive, a criterion imposed on phase model (3). Last, the condition $\sigma_1 \ll 1$ was always satisfied (see appendix C), while for common noise, moderate intensities were obtained.

Figure 5 displays the Lyapunov exponent as a function of stimulus amplitude, derived based on the analysis of MERs, at different site depths and trajectories selected for intraoperative macrostimulation. Overall, the Lyapunov exponent gradually increased with increasing stimulus amplitude. This fact provided further corroboration that the proposed model held the ability to simulate the desynchronizing effect of stimulation. For each case in figure 5, two trajectories traversing the broadest extent of the nucleus (i.e. defined as acceptable by the clinical experts) are examined. The optimal target points according to clinical decision are C 0 (case 1) and L -2.0 (case 4) (table 1). In the aforementioned cases, values of the Lyapunov exponent are for no other site significantly higher than values for the optimal stimulation site ($p < 0.05$), within the trajectory along which the best stimulation effects are obtained. Comparing results between trajectories, there is no site along the alternative trajectory for which the derived exponent is significantly higher than the one corresponding to the finally selected site ($p < 0.05$).

In general, considering as true positive the result obtained under the condition that the derived values of λ were not significantly higher for the nearby sites than the values derived for the optimal stimulation site ($p < 0.05$), the proposed method yielded a sensitivity of 78.57%. Strengthening the condition by including comparative assessment of the Lyapunov exponent between two MER trajectories, the method yielded a sensitivity of 71.43% (table 3).

Figure 8 provides an integrated visualization scheme of the procedure of clinical decision making during DBS surgery, based on the proposed stochastic model. Initially, synchronization index Q was comparatively assessed for the five trajectories (central, anterior, posterior, medial and lateral). Accordingly, the acceptable trajectories could be determined as described in section 2.4.5. Subsequently, values of biomarker Q at specific sites of the acceptable trajectories were employed as one of the inputs (parameters) to the stochastic phase model, while the respective values of biomarker λ actually reflected the output of the model. Eventually, sites where the highest positive values of λ were obtained, were considered as the sites where stimulation yielded the best clinical benefit.

Remarkably, the proposed stochastic model corroborated the increased effectiveness of high frequency stimulation

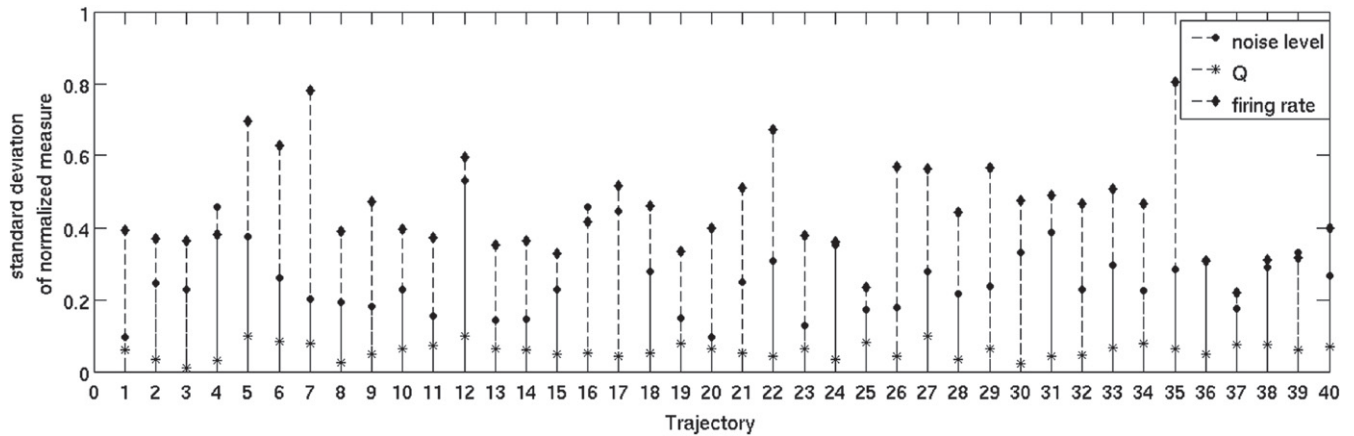


Figure 7. Standard deviation of the normalized firing rate, noise level and multivariate phase synchronization measures within the intraoperatively determined STN length, for 40 trajectories to which a positive detection was ascribed by the clinical experts. Principally, Q displayed significantly higher stability within the STN compared with firing rate and noise level measures ($p < 0.05$).

compared with low frequency stimulation in PD (Rizzone *et al* 2001), (figure 9). Importantly, however, stimulation at beta frequencies did not further synchronize oscillatory activity, as indicated by positive values of the Lyapunov exponent. This observation is in agreement with the study of Tsang *et al* (2012), who suggested that beta frequencies did not worsen PD motor signs.

4. Discussion

Physiologically guided neurosurgery has been adopted by the majority of DBS centers and will apparently continue to be a powerful practice in the field of stereotactic and functional neurosurgery for many years to come (Lozano 2010, Abosch *et al* 2013). Development of related automatic methodologies having the potential to be intraoperatively incorporated, thereby leading to significant reduction of surgical time and optimization of clinical decision making, is therefore of practical importance. Several studies have suggested certain STN detection algorithms, based mainly on combinations of quantitative measures (Falkenberg *et al* 2006, Danish *et al* 2008, Zaidel *et al* 2009, Wong *et al* 2009, Cagnan *et al* 2011, Pinzon-Morales *et al* 2011). Nevertheless, application of a robust single-biomarker approach, having the inherent potential to simplify and accelerate intraoperative nucleus detection, has not been reported in the literature before. Most importantly, to the best of our knowledge, no extensive study has to date been published on an automatic algorithm applicable to the entire electrophysiological procedure, i.e. encompassing both MER and intraoperative stimulation, and pointing to the finally selected site for implantation of the DBS electrode.

Pathological synchronization is considered to be related to the severity of motor impairment in PD (Kühn *et al* 2009, Pogosyan *et al* 2010). Furthermore, there is recent electrophysiological evidence regarding patients with movement disorders but also modeling studies suggesting that alterations in the abnormal discharge pattern of STN neurons and disruption of neuronal synchronization probably explain the

therapeutic mechanism of action of STN-DBS (Carlson *et al* 2010, Walker *et al* 2011, Hauptmann *et al* 2007, Modolo and Beuter 2009, Wilson *et al* 2011, Johnson *et al* 2013). Both of the above facts implicitly point to the possible usefulness of methods from stochastic nonlinear dynamics in the context of clinical decision making during surgical implantation of the DBS electrode. In that vein, in this work, we have attempted to develop a novel integrated approach based on two principal biomarkers, the multivariate phase synchronization index, Q , and the Lyapunov exponent, λ , of a stochastic phase model, for optimal target identification during DBS surgery. To address this goal, we relied on assessment of multi-scale neuronal activity through MER. Essentially, the presence of noise constituted a key factor for the twofold objective of the current study: on the one hand, application of phase synchronization indices had to be robust against the impact of measurement noise, while on the other hand, intrinsic and extrinsic components of the noise were of paramount importance in the phase model employed.

The results of this work signified the high discriminative power of multivariate phase synchronization index Q (as well as of the bivariate phase synchronization indices $\rho_{1,2}$ and $\rho_{1,3}$) in the context of STN localization, a procedure forming the first part of electrophysiological monitoring (Marceglia *et al* 2010). Application of data-driven optimal filtering on the examined signal components (Rossberg *et al* 2004) in combination with NPE (Sun *et al* 2008) ensured remarkable stability of feature evolution inside the nucleus against the presence of noise. To the best of our knowledge a single-biomarker approach displaying similar stability for intraoperative nucleus detection has not been presented in the literature before. This biomarker was subsequently exploited as one of the constituent parameters of the stochastic phase model. Principally, the proposed model held the ability to reproduce the desynchronizing effect of periodic stimulation. This fact was validated through both the invariant measure and the Lyapunov exponent λ of the stochastic phase map. There are two principal reasons that could have contributed to this result. Firstly, selection of a Type-II PRC as the phase sensitivity function to common (extrinsic) noise (Abouzeid

Table 2. Performance of the STN detection methodology.

Index	FPR	FNR	Sensitivity for the STN dorsal border ^a	Sensitivity for the STN ventral border ^a
Q	0%	4.8%	100%	92%
$\rho_{1,2}$	0%	4.8%	100%	92%
$\rho_{1,3}$	0%	4.8%	100%	92%
$\rho_{2,3}$	—	—	—	—

^a Within 0.5 mm accuracy of the current gold standard.

Table 3. Performance of the stochastic model under two principal conditions^{a,b} for designation of the optimal stimulation site.

Measure	Sensitivity
λ^a	78.57%
λ^b	71.43%

^a Values of λ within the optimal trajectory were for no other site significantly higher than the values derived for the optimal stimulation site (according to clinical decision) ($p < 0.05$).

^b In addition to a, there was no site along the alternative trajectory for which the derived exponent was significantly higher than the one corresponding to the finally selected site ($p < 0.05$).

and Ermentrout 2009), guaranteed to a great extent that the model would simulate the pathological synchronous state in the absence of any stimulus, yielding a negative Lyapunov exponent. On the contrary, a Type- I PRC would rather be linked to the normal desynchronized state (Farries and Wilson 2012). Secondly, application of a type 0 PRC, potentially optimal for stochastic desynchronization (Hata *et al* 2011), contributed to simulation of one of the hypothetical mechanisms of high frequency stimulation. Eventually, on the basis of the simulations proposed, a neurosurgeon may be able to determine the optimal stimulation sites with enhanced sensitivity.

The proposed phase model was developed incorporating multiple factors affecting neuronal dynamics: neuronal coupling, intrinsic independent and extrinsic common noise sources, and periodic forcing. Thus, the derived Lyapunov exponent, λ , was combinatorially correlated with the set of the respective parameter values and not uniquely determined by multivariate phase synchronization index, Q . Some previous studies (Tass *et al* 2006, Nabi *et al* 2013) have suggested similar models in the framework of desynchronizing stimulation, yet only embodying the effect of intrinsic noise, disregarding extrinsic noise sources (Teramae and Tanaka 2004). Additionally, the above models did not consider the phase dependence of the noise (Ermentrout and Saunders 2006), thus noise forcing was not necessarily multiplicative (Ly and Ermentrout 2011). Most importantly, in this work, intending to implement a more realistic model, we have considered common noise as colored, namely as an Ornstein–Uhlenbeck process with specific correlation time (Galán 2009). For this reason, we required a transformation of the initial phase

model to a white noise Langevin equation, introducing the effective drift and diffusion coefficients (Nakao *et al* 2010).

In what concerns the simplifications and limitations of the presented approach, first and foremost, we do not claim that application of the proposed method can be regarded as a complete substitute for functional stimulation techniques. Assessment of stimulation-induced side effects is undoubtedly a significant factor in clinical decision making during intraoperative macrostimulation (Schlaier *et al* 2013) and was not quantitatively incorporated in this study. However, it should be pointed out that intraoperative quantification of the therapeutic window (intensity threshold for side effects/intensity threshold for clinical effects) depends to a large extent on the assessment of the therapeutic effects of stimulation (Marceglia *et al* 2010). Besides, a relatively low threshold for the appearance of clinical effects is evidently associated with reduced probability that a side-effect will be evoked at the same intensity, since the most common side effects induced by STN-DBS, i.e. pyramidal tract side effects, occur at a median amplitude of 4.8 V (Tommasi *et al* 2008). We believe that the above facts in combination with the good consistency of the proposed scheme with expert annotations, assign a specific value to the presented approach. Considering further the limitations of this work, the fact that we do not isolate single units prior to feature evaluation would likely have influenced the results of our study. Still, similar approaches in the context of automatic algorithms for nucleus localization have been adopted by other studies as well (Wong *et al* 2009, Cagnan *et al* 2011). Last, we should note that we did not hereby characterize to what extent simulations of the stochastic model would be distinct for different types of phase response functions to the noise sources. The possible disparities remain to be elucidated in future work.

Further future perspectives include assessment of the predictive value of the stochastic model considering data from more patients and other clinical implementations of DBS (Mallet *et al* 2008, Chabardès *et al* 2013, Fytigoridis *et al* 2012). Particularly, in patients with obsessive-compulsive disorder, evidence that the efficacy of STN-DBS probably lies in alteration of the abnormal bursty activity pattern observed in the associative-limbic part of the nucleus (Piallat *et al* 2011, Welter *et al* 2011) implicitly indicates possible suitability of the current approach for DBS electrode localization. At the same time, appropriate modification of the presented methodology to include quantitative measures reflecting the evaluation of stimulation-induced side effects is expected to enhance its practicability in the surgical procedure. Furthermore, in light of evidence pointing to a possible correlation between intra- and postoperative outcomes of clinical evaluation (Xie *et al* 2010), proper adaptation of the proposed scheme to DBS programming could potentially facilitate clinical decision making postoperatively. Finally, due to the considerably realistic nature of the stochastic phase model employed, model variations could prove useful for investigating the clinical efficacy induced by alternative patterns of DBS (Brocker *et al* 2013), opening an intriguing perspective for future study.

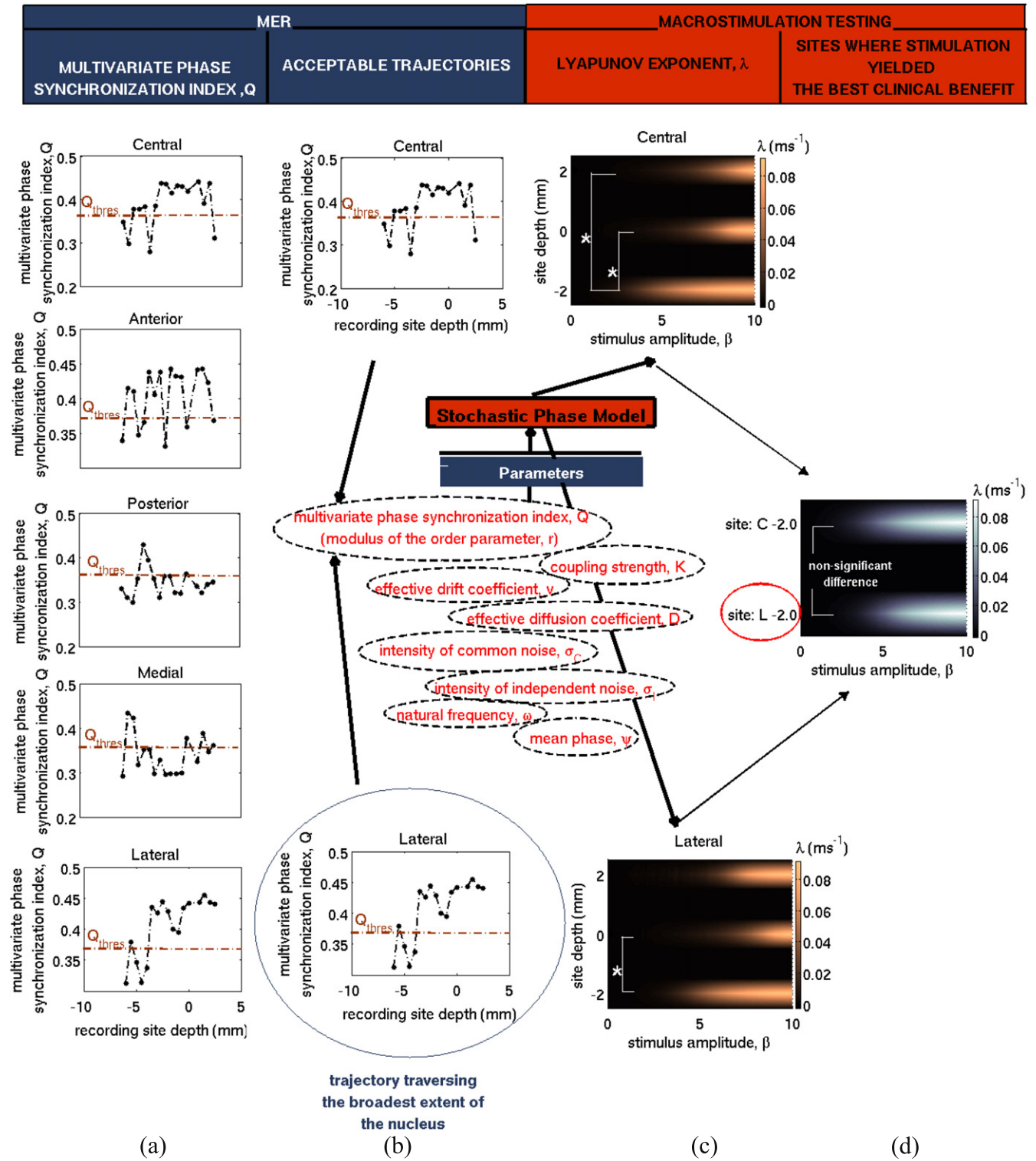


Figure 8. The proposed scheme for clinical decision making during DBS surgery for PD, based on the stochastic dynamical model. (a) Assessment of the multivariate phase synchronization index Q across five trajectories of left STN, case 4. (b) Determination of the two acceptable trajectories, including the one traversing the broadest extent of the nucleus. Biomarker Q was subsequently used as one of the constituent parameters of the stochastic phase model through which we defined (c) the Lyapunov exponent, λ , as a function of stimulus amplitude β , at three pre-selected recording sites, for both acceptable trajectories. Asterisks denote significant differences. (d) Sites where the highest values of λ were obtained according to (c) for each of the acceptable trajectories. At these sites, values of λ between the two trajectories were not significantly different. Circled is the site finally selected by the clinical experts.

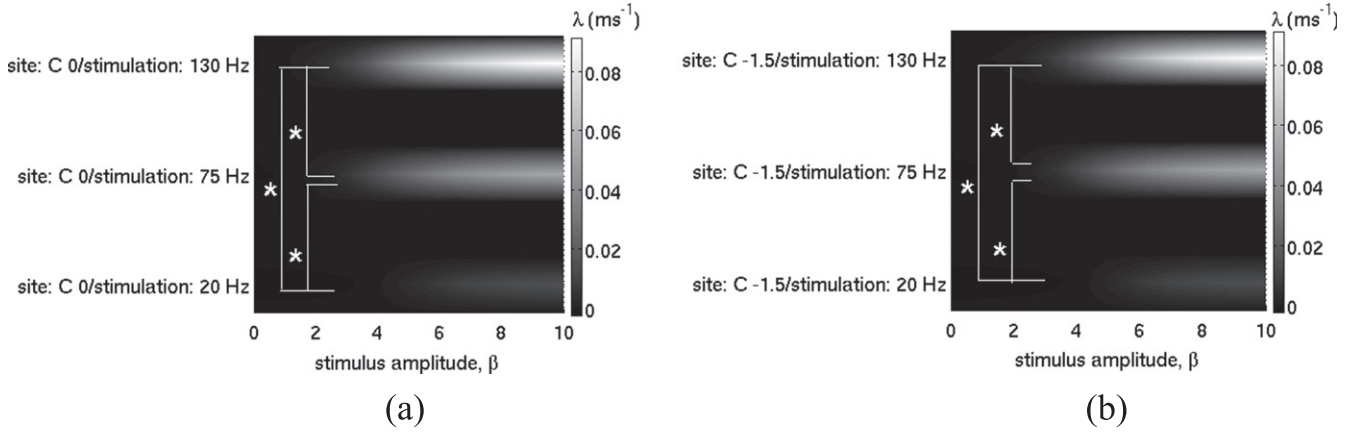


Figure 9. Increased effectiveness of high frequency stimulation corroborated by the stochastic phase model. The Lyapunov exponent λ as a function of stimulus amplitude β , at sites (a) C 0, right STN, case 7 and (b) C -1.5, right STN, case 9, for three different stimulation frequencies (20 Hz, 75 Hz and 130 Hz).

Appendix A. Bivariate phase synchronization index

Due to the nonstationarity of the data, we performed the analysis over a sliding window of 1 s ($M = 1000$ samples) (Hurtado *et al* 2004) and computed for every sampling point t_k the distribution of the relative phase series $\Delta\phi$ of the interacting oscillators, using

$$I = \exp(0.626 + 0.4 \ln(M - 1)) = 30$$

bins (Gross *et al* 2000). The entropy of the distribution was calculated as

$$h(t_k) = - \sum_{i=1}^I p_i(k) \ln p_i(k), \quad (\text{A.1})$$

where p_i is the probability corresponding to the i th bin. The synchronization index used was equal to the normalized entropy of the distribution

$$\rho(t_k) = \frac{h_{\max} - h(t_k)}{h_{\max}}, \quad (\text{A.2})$$

where $h_{\max} = \ln I$. Obviously, $0 \leq \rho(t_k) \leq 1$, where the value $\rho(t_k) = 0$ corresponds to a uniform distribution (unsynchronized time series), whereas the value $\rho(t_k) = 1$ corresponds to perfect synchronization.

Appendix B. Determination of phase sensitivity functions

Taking into consideration that for weak Gaussian common driving noise, a Type-II PRC is optimal for stochastic synchronization (Abouzeid and Ermentrout 2009), we use this shape for the phase sensitivity to common noise in order to simulate the state of pathological synchronization in PD. A Type-I PRC is selected for the phase sensitivity to independent noise. Both PRCs are normalized as $\sqrt{\int_0^1 R^2(\phi) d\phi} = 1$.

Accordingly we consider

$$R_C(\phi) = \sqrt{2} (-\sin(2\pi\phi)) \quad (\text{B.1})$$

$$R_I(\phi) = \sqrt{\frac{2}{3}} (1 - \cos(2\pi\phi)). \quad (\text{B.2})$$

Differently, there is evidence that the type 0 PRC may be optimal for stochastic desynchronization (Hata *et al* 2011). Hence, in order to simulate the desynchronizing effect of DBS we consider $\Delta(\phi, 0) = 0$ and

$$\Delta(\phi, \beta) = \begin{cases} \phi e^{(10-\beta)(\phi-0.5)} & 0 < \phi \leq 0.5 \\ (\phi - 1) e^{-(10-\beta)(\phi-0.5)} & 0.5 \leq \phi < 1 \end{cases}, \quad (\text{B.3})$$

where $0 < \beta \leq 10$.

Appendix C. Evaluation of the intensity of independent noise

Let $\rho(\phi, t)$ represent the probability density function of phases at time t . The corresponding Fokker–Planck equation is (Gardiner 1985)

$$\begin{aligned} \frac{\partial \rho}{\partial t} = & - \frac{\partial}{\partial \phi} \{ [\omega + Kr \sin(2\pi(\psi - \phi)) + v \\ & + \frac{\sigma_I}{2} R'_I(\phi) (\sigma_I R_I(\phi) + \sqrt{D}) \rho \} \\ & + \frac{1}{2} \frac{\partial^2}{\partial \phi^2} \{ (\sigma_I R_I(\phi) + \sqrt{D})^2 \rho \}, \end{aligned} \quad (\text{C.1})$$

with periodic boundary condition

$$\rho(0, t) = \rho(1, t). \quad (\text{C.2})$$

Extending the definition of the phase from $\phi \in [0,1)$ to $\phi \in \mathfrak{R}$ and considering $\sigma_1 \ll 1$ we obtain the following approximations (Ly and Ermentrout 2011)

$$\begin{aligned} R_I(\phi) & \approx R_I(t) \text{ and} \\ Kr \sin(2\pi(\psi - \phi)) & \approx Kr \sin(2\pi(\psi - t)). \end{aligned} \quad (\text{C.3})$$

The Fokker–Planck equation for the corresponding probability density function $\zeta(\phi, t)$ is

$$\begin{aligned} \frac{\partial \zeta}{\partial t} = & -[\omega + Kr \sin(2\pi(\psi - t)) + \nu \\ & + \frac{\sigma_I}{2} R_I'(t)(\sigma_I R_I(t) + \sqrt{D})] \frac{\partial \zeta}{\partial \phi} \\ & + \frac{(\sigma_I R_I(t) + \sqrt{D})^2}{2} \frac{\partial^2 \zeta}{\partial \phi^2} \end{aligned} \quad (C.4)$$

$$\zeta(\phi, 0) = \delta(\phi), \quad \phi \in \mathfrak{R}. \quad (C.5)$$

An analytic solution to (C.4) is

$$\begin{aligned} \zeta(\phi, t) = & \frac{1}{\left(2\pi \left(\sigma_I^2 \int_0^t R_I^2(s) ds + 2\sigma_I \sqrt{D} \int_0^t R_I(s) ds + Dt\right)\right)^{1/2}} \\ & \times \exp \left(- \frac{\left((\omega + \nu)t + \frac{1}{2\pi} Kr \cos(2\pi(\psi - t)) - \phi \right)^2 + \frac{\sigma_I^2}{4} R_I^2(t) + \frac{\sigma_I \sqrt{D}}{2} R_I(t)}{2 \left(\sigma_I^2 \int_0^t R_I^2(s) ds + 2\sigma_I \sqrt{D} \int_0^t R_I(s) ds + Dt\right)} \right). \end{aligned} \quad (C.6)$$

Respectively, the first passage time distribution is simply

$$z(t) = \zeta(1, t). \quad (C.7)$$

Finally, maximization of the log likelihood function L over σ_I , yields an estimate for σ_I (Nesse and Clark 2010):

$$\begin{aligned} \frac{d}{d\sigma_I} L(\sigma_I | \{\Delta t_i\}, \nu, K, r, D) = & \frac{d}{d\sigma_I} \\ & \times \sum_i \ln z(\Delta t_i | \sigma_I, \nu, K, r, D) = 0, \end{aligned} \quad (C.8)$$

where $\{\Delta t_i\}$ are the interspike interval data.

References

Abosch A, Timmermann L, Bartley S, Rietkerk H G, Whiting D, Connolly P, Lanctin D and Hariz M I 2013 An international survey of deep brain stimulation procedural steps *Stereotact. Funct. Neurosurg.* **91** 1–11

Abouzeid A and Ermentrout B 2009 The type II phase resetting curve is optimal for stochastic synchrony *Phys. Rev. E* **80** 011911

Allefeld C and Kurths J 2004 An approach to multivariate phase synchronization analysis and its application to event-related potentials *Int. J. Bifurcation Chaos* **14** 417–26

Allefeld C, Müller M and Kurths J 2007 Eigenvalue decomposition as a generalized synchronization cluster analysis *Int. J. Bifurcation Chaos* **17** 3493–7

Benabid A L 2003 Deep brain stimulation for Parkinson’s disease *Curr. Opin. Neurobiol.* **13** 696–706

Benabid A L, Chabardès S, Mitrofanis J and Pollak P 2009 Deep brain stimulation of the subthalamic nucleus for the treatment of Parkinson’s disease *Lancet Neurol.* **8** 67–81

Benabid A L, Pollak P, Gross C, Hoffmann D, Benazzouz A, Gao D M, Laurent A, Gentil M and Perret J 1994 Acute and long-term effects of subthalamic nucleus stimulation in Parkinson’s disease *Stereotact. Funct. Neurosurg.* **62** 76–84

Bour L J, Contarino M F, Foncke E M, de Bie R M, van den Munckhof P, Speelman J D and Schuurman P R 2010 Long-term experience with intraoperative microrecording during DBS neurosurgery in STN and GPi *Acta Neurochir. (Wien)* **152** 2069–77

Boviatsis E J, Stavrinou L C, Themistocleous M, Kouyialis A T and Sakas D E 2010 Surgical and hardware complications of deep brain stimulation. A seven-year experience and review of the literature *Acta Neurochir. (Wien)* **152** 2053–62

Brocker D T, Swan B D, Turner D A, Gross R E, Tatter S B, Miller Koop M, Bronte-Stewart H and Grill W M 2013 Improved efficacy of temporally nonregular deep brain stimulation in Parkinson’s disease *Exp. Neurol.* **239** 60–7

Cagnan H, Dolan K, He X, Contarino M F, Schuurman R, van den Munckhof P, Wadman W J, Bour L and Martens H C F 2011 Automatic subthalamic nucleus detection from microelectrode recordings based on noise level and neuronal activity *J. Neural Eng.* **8** 1–9

Carlson J D, Cleary D R, Cetas J S, Heinricher M M and Burchiel K J D 2010 Deep brain stimulation does not silence neurons in subthalamic nucleus in Parkinson’s patients *J. Neurophysiol.* **103** 962–7

Carmeli C, Knyazeva M G, Innocenti G M and De Feo O 2005 Assessment of EEG synchronization based on state-space analysis *NeuroImage* **25** 339–54

Chabardès S, Polosan M, Krack P, Bastin J, Krainik A, David O, Bougerol T and Benabid A L 2013 Deep brain stimulation for obsessive compulsive disorder: subthalamic nucleus target *World Neurosurg.* **80** e1–S31

Danish S F, Baltuch G H, Jaggi J L and Wong S 2008 Determination of subthalamic nucleus location by quantitative analysis of despiked background neural activity from microelectrode recordings obtained during deep brain stimulation surgery *J. Clin. Neurophysiol.* **25** 98–103

Dolan K, Martens H C F, Schuurman P R and Bour L J 2009 Automatic noise-level detection for extra-cellular microelectrode recordings *Med. Biol. Eng. Comput.* **47** 791–800

Ermentrout B and Saunders D 2006 Phase resetting and coupling of noisy neural oscillators *J. Comput. Neurosci.* **20** 179–90

Falkenberg J H, McNames J, Favre J and Burchiel K J 2006 Automatic analysis and visualization of microelectrode recording trajectories to the subthalamic nucleus: preliminary results *Stereotact. Funct. Neurosurg.* **84** 35–44

Farries M A and Wilson C J 2012 Phase response curves of subthalamic neurons measured with synaptic input and current injection *J. Neurophysiol.* **108** 1822–37

Fytogoridis A, Åström M, Wårdell K and Blomstedt P 2012 Stimulation-induced side effects in the posterior subthalamic area: distribution, characteristics and visualization *Clin. Neurol. Neurosurg.* **115** 65–71

Galán R 2009 Analytical calculation of the frequency shift in phase oscillators driven by colored noise: Implications for electrical engineering and neuroscience *Phys. Rev. E* **80** 036113

Gardiner C 1985 *Handbook of Stochastic Methods* (Berlin: Springer)

Gross J, Tass P A, Salenius S, Hari R, Freund H J and Schnitzler A 2000 Cortico-muscular synchronization during isometric muscle contraction in humans as revealed by magnetoencephalography *J. Physiol.* **527** 623–31

Gross R E, Krack P, Rodriguez-Oroz M C, Rezaï A R and Benabid A L 2006 Electrophysiological mapping for the

- implantation of deep brain stimulators for Parkinson's disease and tremor *Mov. Disord.* **21** S259–83
- Hata S, Arai K, Galán R F and Nakao H 2011 Optimal phase response curves for stochastic synchronization of limit-cycle oscillators by common Poisson noise *Phys. Rev. E* **84** 016229
- Hauptmann C, Popovych O and Tass P A 2007 Desynchronizing the abnormally synchronized neural activity in the subthalamic nucleus: a modeling study *Expert Rev. Med. Devices* **4** 633–50
- Hurtado J M, Rubchinsky L L and Sigvardt K A 2004 Statistical method for detection of phase-locking episodes in neural oscillations *J. Neurophysiol.* **91** 1883–98
- Johnson M D *et al* 2013 Neuromodulation for brain disorders: challenges and opportunities *IEEE Trans. Biomed. Eng.* **60** 610–24
- Kühn A A, Trottenberg T, Kivi A, Kupsch A, Schneider G H and Brown P 2005 The relationship between local field potential and neuronal discharge in the subthalamic nucleus of patients with Parkinson's disease *Exp. Neurol.* **194** 212–20
- Kühn A A, Tsui A, Aziz T, Ray N, Brücke C, Kupsch A, Schneider G H and Brown P 2009 Pathological synchronization in the subthalamic nucleus of patients with Parkinson's disease relates to both bradykinesia and rigidity *Exp. Neurol.* **215** 380–7
- Kuramoto Y 1984 *Chemical Oscillations, Waves, and Turbulence* (New York: Springer)
- Limousin P, Pollak P, Benazzouz A, Hoffmann D, Le Bas J F, Broussolle E, Perret J E and Benabid A L 1995 Effect on parkinsonian signs and symptoms of bilateral subthalamic nucleus stimulation *Lancet* **345** 91–5
- Logothetis N K 2002 The neural basis of the blood-oxygen-level-dependent functional magnetic resonance imaging signal *Phil. Trans. R. Soc. London B* **357** 1003–37
- Lozano A M 2010 Deep brain stimulation for Parkinson disease *J. Neurosurg.* **112** 477–8
- Lozano A M, Snyder B J, Hamani C, Hutchison W D and Dostrovsky J O 2010 Basal ganglia physiology and deep brain stimulation *Mov. Disord.* **25** S71–5
- Ly C and Ermentrout G B 2011 Analytic approximations of statistical quantities and response of noisy oscillators *Physica D* **240** 719–31
- Mallet L *et al* 2008 Subthalamic nucleus stimulation in severe obsessive-compulsive disorder *N. Engl. J. Med.* **359** 2121–34
- Marceglia S, Mrakic-Sposta S, Tommasi G, Bartolomei L, Foresti C, Valzania F, Galati S, Stefani A, Tamma F and Priori A 2010 Multicenter study report: electrophysiological monitoring procedures for subthalamic deep brain stimulation surgery in Parkinson's disease *Neurol. Sci.* **31** 449–57
- Mitzdorf U 1987 Properties of the evoked potential generators: current source-density analysis of visually evoked potentials in the cat cortex *Int. J. Neurosci.* **33** 33–59
- Modolo J and Beuter A 2009 Linking brain dynamics, neural mechanisms and deep brain stimulation in Parkinson's disease: an integrated perspective *Med. Eng. Phys.* **31** 615–23
- Moran A, Bergman H, Israel Z and Bar-Gad I 2008 Subthalamic nucleus functional organization revealed by parkinsonian neuronal oscillations and synchrony *Brain* **131** 3395–409
- Moran A and Bar-Gad I 2010 Revealing neuronal functional organization through the relation between multi-scale oscillatory extracellular signals *J. Neurosci. Methods* **186** 116–29
- Nabi A, Mirzadeh M, Gibou F and Moehlis J 2013 Minimum energy desynchronizing control for coupled neurons *J. Comput. Neurosci.* **34** 259–71
- Nakao H, Teramae J, Goldobin D and Kuramoto Y 2010 Effective long-time phase dynamics of limit-cycle oscillators driven by weak colored noise *Chaos* **20** 033126
- Nesse W H and Clark G A 2010 Relative spike timing in stochastic oscillator networks of the hermissenda eye *Biol. Cybern.* **102** 389–412
- Nesse W H, Clark G A and Bressloff P C 2007 Spike patterning of a stochastic phase model neuron given periodic inhibition *Phys. Rev. E* **75** 031912
- Noutsos D and Tsatsomeros M 2008 Reachability and holdability of nonnegative states *SIAM J. Matrix Anal. Appl.* **30** 700–12
- Novak P, Przybyszewski A W, Barborica A, Ravin P, Margolin L and Pilitsis J G 2011 Localization of the subthalamic nucleus in Parkinson disease using multiunit activity *J. Neurol. Sci.* **310** 44–9
- Piallat B *et al* 2011 Subthalamic neuronal firing in obsessive-compulsive disorder and Parkinson disease *Ann. Neurol.* **69** 793–802
- Pikovsky A, Rosenblum M G and Kurths J 2001 *Synchronization: A Universal Concept in Nonlinear Sciences* (Cambridge: Cambridge University Press)
- Pinzon-Morales R D, Orozco-Gutierrez A A and Castellanos-Dominguez G 2011 Novel signal-dependent filter bank method for identification of multiple basal ganglia nuclei in parkinsonian patients *J. Neural Eng.* **8** 1–10
- Pogosyan A, Yoshida F, Chen C C, Martinez-Torres I, Foltyniec T, Limousin P, Zrinzo L, Hariz M I and Brown P 2010 Parkinsonian impairment correlates with spatially extensive subthalamic oscillatory synchronization *Neuroscience* **171** 245–57
- Pollak P, Krack P, Fraix V, Mendes A, Moro E, Chabardes S and Benabid A L 2002 Intraoperative micro- and macrostimulation of the subthalamic nucleus in Parkinson's disease *Mov. Disord.* **17** S155–61
- Polychronaki G E 2011 Development of methodologies based on non-linear measures for the analysis of data from epileptic patients *Doctoral dissertation* National Technical University of Athens Greece
- Reck C, Maarouf M, Wojtecki L, Groiss S J, Florin E, Sturm V, Fink G R, Schnitzler A and Timmermann L 2012 Clinical outcome of subthalamic stimulation in Parkinson's disease is improved by intraoperative multiple trajectories microelectrode recording *J. Neurol. Surg. A* **73** 377–86
- Rizzone M, Lanotte M, Bergamasco B, Tavella A, Torre E, Faccani G, Melcarne A and Lopiano L 2001 Deep brain stimulation of the subthalamic nucleus in Parkinson's disease: effects of variation in stimulation parameters *J. Neurol. Neurosurg. Psychiatry* **71** 215–9
- Rossberg A G, Bartholomé K and Timmer J 2004 Data-driven optimal filtering for phase and frequency of noisy oscillations: Application to vortex flow metering *Phys. Rev. E* **69** 016216
- Sakas D E, Kouyialis A T, Boviatsis E J, Panourias I G, Stathis P and Tagaris G 2007 Technical aspects and considerations of deep brain stimulation surgery for movement disorders *Acta Neurochir. Suppl.* **97** 163–70
- Schaltenbrand G and Wahren W 1977 *Atlas for Stereotaxy of the Human Brain* (Stuttgart: Thieme)
- Schlaier J R, Habermeyer C, Janzen A, Fellner C, Hochreiter A, Proescholdt M, Brawanski A and Lange M 2013 The influence of intraoperative microelectrode recordings and clinical testing on the location of final stimulation sites in deep brain stimulation for Parkinson's disease *Acta Neurochir. (Wien)* **155** 357–66
- Starr P A 2010 Deep brain stimulation for Parkinson disease *J. Neurosurg.* **112** 477–8
- Strogatz S H 2000 From Kuramoto to Crawford: exploring the onset of synchronization in populations of coupled oscillators *Physica D* **143** 1–20
- Sun J, Zhang J, Zhou J, Xu X and Small M 2008 Detecting phase synchronization in noisy data from coupled chaotic oscillators *Phys. Rev. E* **77** 046213

- Takens F 1981 Detecting strange attractors in turbulence *Dynamical Systems and Turbulence (Lecture Notes in Mathematics vol 898)* ed D A Rand and L S Young (Berlin: Springer) pp 365–81
- Tass P, Rosenblum M G, Weule J, Kurths J, Pikovsky A, Volkmann J, Schnitzler A and Freund H–J 1998 Detection of n:m phase locking from noisy data: application to magnetoencephalography *Phys. Rev. Lett.* **81** 3291–4
- Tass P A, Hauptmann C and Popovych O V 2006 Development of therapeutic brain stimulation techniques with methods from nonlinear dynamics and statistical physics *Int. J. Bifurcation Chaos* **16** 1889–911
- Teramae J N and Tanaka D 2004 Robustness of the noise-induced phase synchronization in a general class of limit cycle oscillators *Phys. Rev. Lett.* **93** 204103
- Tommasi G, Krack P, Fraix V, Le Bas J F, Chabardes S, Benabid A L and Pollak P 2008 Pyramidal tract side effects induced by deep brain stimulation of the subthalamic nucleus *J. Neurol. Neurosurg. Psychiatry* **79** 813–9
- Tsang E W *et al* 2012 Subthalamic deep brain stimulation at individualized frequencies for Parkinson disease *Neurology* **78** 1930–8
- Tsirogiannis G L, Tagaris G A, Sakas D and Nikita K S 2010 A population level computational model of the basal ganglia that generates parkinsonian local field potential activity *Biol. Cybern.* **102** 155–76
- Walker H C, Watts R L, Schrandt C J, Huang H, Guthrie S L, Guthrie B L and Montgomery E B Jr 2011 Activation of subthalamic neurons by contralateral subthalamic deep brain stimulation in Parkinson disease *J. Neurophysiol.* **105** 1112–21
- Weinberger M, Mahant N, Hutchison W D, Lozano A M, Moro E, Hodaie M, Lang A E and Dostrovsky J O 2006 Beta oscillatory activity in the subthalamic nucleus and its relation to dopaminergic response in Parkinson’s disease *J. Neurophysiol.* **96** 3248–56
- Welter M L *et al* 2011 Basal ganglia dysfunction in OCD: subthalamic neuronal activity correlates with symptoms severity and predicts high-frequency stimulation efficacy *Transl. Psychiatry* **1** e5
- Wilson C J, Beverlin B 2nd and Netoff T 2011 Chaotic desynchronization as the therapeutic mechanism of deep brain stimulation *Front. Syst. Neurosci.* **5** 1–11
- Winfree A T 2001 *The Geometry of Biological Time* (New York: Springer)
- Wong S, Baltuch G H, Jaggi J L and Danish S F 2009 Functional localization and visualization of the subthalamic nucleus from microelectrode recordings acquired during DBS surgery with unsupervised machine learning *J. Neural Eng.* **6** 1–11
- Xie J, Adamec D, Decullier E, Bin-Dorel S, Mertens P, Polo G, Poisson A, Broussolle E and Thobois S 2010 Do the effects measured by intraoperative and postoperative STN macrostimulation in Parkinson’s disease match? *J. Neurol.* **257** 1453–6
- Yamanobe T and Pakdaman K 2002 Response of a pacemaker neuron model to stochastic pulse trains *Biol. Cybern.* **86** 155–66
- Zaidel A, Spivak A, Shpigelman L, Bergman H and Israel Z 2009 Delimiting subterritories of the human subthalamic nucleus by means of microelectrode recordings and a hidden Markov model *Mov. Disord.* **24** 1785–93